

# Numerical study of the first Gabor lens prototype

Titus-Stefan Dascalu

January 18, 2021

---

## Abstract

In the process of designing the Gabor lens for the Laser-hybrid Accelerator for Radiobiological Applications (LhARA), a study of the stability of the lens was undertaken using a PIC code. The configuration of the lens was found to lead to a stable electron cloud filling the lens only partially under the proper tuning of the strength of the confining fields. Several instabilities were observed in the simulations and the effect of each of them was studied for six proton pencil beams propagating through the plasma. An instability with dipole structure was associated with the formation of ring spots from the pencil beams. A simplified model was created with the essential features of the dipole instability and a particle-tracking code was used to reproduce the images taken during a beam test of the first prototype of the lens.

---

## Contents

<b>1</b>	<b>Introduction</b>	<b>1</b>
1.1	Beam test setup . . . . .	2
<b>2</b>	<b>Plasma simulations</b>	<b>2</b>
2.1	Stable regime . . . . .	2
2.2	Unstable regime . . . . .	5
2.2.1	Beam tracking . . . . .	5
2.2.2	Diocotron instability . . . . .	6
2.2.3	Electron ring . . . . .	7
2.2.4	‘Dipole instability’ . . . . .	7
<b>3</b>	<b>Alternative model of the instability</b>	<b>9</b>
3.1	Electric field map . . . . .	10
3.2	Particle tracking . . . . .	11
3.3	Results . . . . .	11
<b>4</b>	<b>Conclusion</b>	<b>13</b>
	<b>References</b>	<b>16</b>

## 1 Introduction

One critical component of LhARA, the Laser-hybrid Accelerator for Radiobiological Applications, is the space-charge lens which enables the capture and focusing of the ions produced by the laser-driven source. In the development of LhARA, it is important to prove that such a plasma lens can be operated in a stable regime with the designed focusing strengths. The current design of LhARA employs five lenses, three of which ensure the energy selection.

Several plasma instabilities have been observed experimentally to disrupt the ion beam [1–4]. To investigate the origin of the instabilities and how to avoid them, a particle-in-cell (PIC) code, VSim [5], was used to simulate the dynamics of the non-neutral plasma confined by the lens. For each type of instability observed, its effect on a proton beam was studied by tracking the protons through the electron cloud. Simulating both the plasma and the proton beam with the PIC code is computationally expensive,

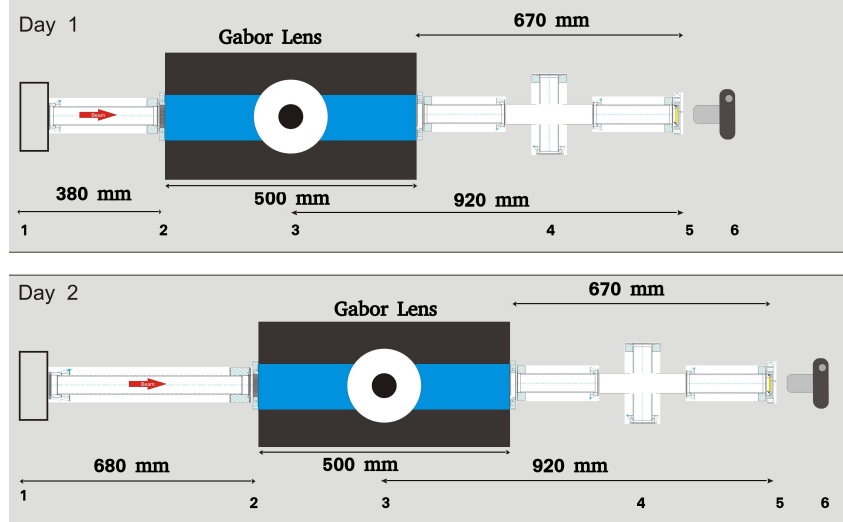


Figure 1: Schematic of the beam test setup during the Day 1 (top) and Day 2 (bottom) of beam operation. The setup shows the position of the Gabor lens, the beam pipes, the aperture and the phosphor screen.

but achievable. A faster alternative method was devised by generating a time-dependent idealised electric field map to represent the space-charge through which the protons were tracked using BDSIM [6].

A first prototype of a space-charge lens for LhARA was built at Imperial and tested with a proton beam. The initial pencil beams were focused into ring shapes with several distinctive features which suggest that the confined plasma was unstable during the measurements. The formation of the rings was reproduced in simulations with the PIC code and a model of the plasma was created to account for some of the features of the rings. As the laser-driven ion beams are highly divergent, it is necessary for the lens to achieve a short focal length, and, thus, a high electron density. Matching the measurements with the simulations leads to an estimation of the plasma densities achieved with the first prototype of the lens.

### 1.1 Beam test setup

A brief description of the experimental setup from the beam test of the first prototype of the Gabor lens is given in this subsection. The lens was operated with a pencil beam of 1.4 MeV protons over the course of two days. During each day, a different arrangement was used as shown on Fig. 1.

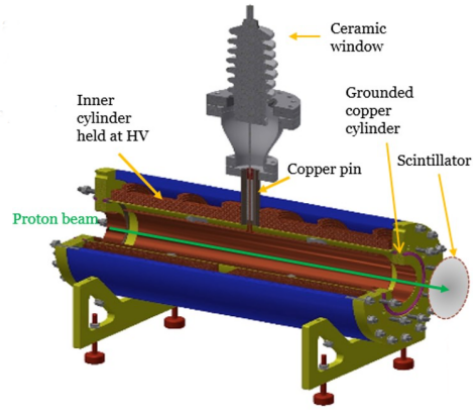
For the numerical simulations described in the following sections, the Day 2 setup was reproduced with the phosphor screen placed at a distance of 670 mm downstream of the Gabor lens. The active scintillator area of the screen had a diameter of 46 mm. Between the initial beam pipe and the lens, an aperture was placed to split the incoming pencil beam into many individual beamlets, each with a diameter of 2 mm. The configuration used in Day 2 allowed six beam spots to be imaged on the phosphor screen. Thus, the following numerical simulations investigate the propagation of six beamlets through various plasma configurations inside the lens.

## 2 Plasma simulations

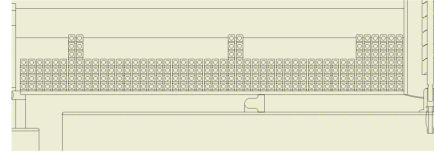
### 2.1 Stable regime

The geometry of the first lens prototype was reproduced in VSim according to the engineering drawings. The model included the central anode, two end electrodes, and the vacuum tube with the end flanges. The width of the walls of the anode and end electrodes was set to double that from the drawings to ensure a proper meshing of these surfaces.

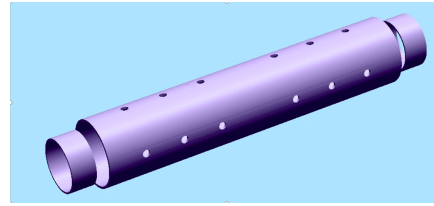
To model the lens accordingly, the configuration of the coil together with all the metallic surfaces were replicated separately by using a finite element analysis package FEMM [7]. The software is used to solve 3D axisymmetric linear magnetostatic problems with a low computational cost. For the studies presented here, the package was used to obtain a 3D magnetic field map starting from the value of the current through the coil (Fig. 3). The field map was then loaded into VSim as the longitudinally



(a) Engineering drawing

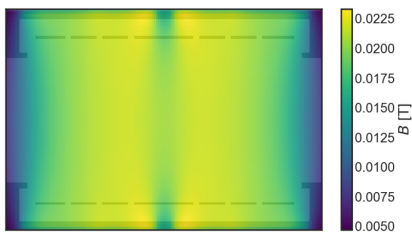


(b) One half of the pancake coils

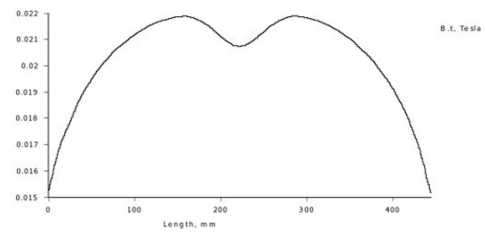


(c) The central anode and the two end electrodes as built in VSim

Figure 2: Previous design and prototype of the Gabor lens.



(a) Longitudinal cross-section



(b) Magnetic flux density on central axis

Figure 3: Magnetic field map obtained with FEMM for the coil configuration shown in Fig. 2 and a coil current of 20 A.

confining magnetic field with the help of a regular grid interpolator and the interface between Python and VSim.

The main plasma parameters and lens specifications used in the simulations are given in Table 1. The anode potential was matched to the average magnetic field according to the work function of the lens [8]

$$V_A = \frac{eR_A^2}{8m_e} B^2 \quad (1)$$

H<sub>2</sub>O was assumed to be the most probable background residual gas. It was introduced in the simulation as a neutral fluid with three interactions possible with the surrounding electrons: elastic collision, impact excitation, and impact ionisation. The corresponding cross-sections were obtained from [9] and [10]. Furthermore, secondary electron emission was included from the surface of the anode and end electrodes. Both the electrons and the ions produced in the impact ionisation could be absorbed at any of the metallic surfaces, as well as at the entry and exit plane of the lens inside the beam-pipe. A typical simulation requires a running time of about 12 hours on 20 cores to simulate the plasma for a time interval of 10  $\mu$ s. VSim was run on the HPC cluster SCARF [11].

**Solver** The two solvers available in VSim were compared against each other in terms of the time it takes to simulate the plasma for 1  $\mu$ s. The electromagnetic solver required a significantly reduced computation time for advancing the plasma by one time step. However, the size of the time step required to achieve convergence was three orders of magnitude smaller than the time step used by the electrostatic solver. Overall, the electrostatic Poisson solver was found to run faster for the grid size and plasma parameters chosen.

**Boundary Conditions** The simulation volume was bounded by Dirichlet boundary conditions with the voltage set to 0 V. The vacuum tube was assumed to fill the full space between its inner cylindrical surface and the planes that enclose the simulation volume. A perfect electric conductor (PEC) material with Dirichlet boundary conditions was used for the anode and the two end tubes, thus allowing the voltage on the electrodes to be specified.

**Initial Conditions** Two different assumptions were used to define the initial distribution of the electron cloud.

- (i) The first method was to assume that the plasma starts from thermal equilibrium. A temperature  $T = 100$  eV was chosen to match previous observations and simulations [3]. The velocity components for each electron were considered to be independent and were sampled from a Maxwellian distribution. The electron density was assumed to be constant.

If the plasma initially occupies only a small volume near the middle plane of the lens, the electrons were seen to flow towards the two ends of the lens until an 'equilibrium length' was reached as in Figure 8(a). If the entire inner volume of the anode is filled with electrons at the initial time step of the simulation, two waves were seen to propagate from the edges of the plasma column towards the centre. The waves continued to propagate forwards and backwards for the entire duration of the simulation. To avoid the formation of these plasma waves, the electrons had to be initialised such that the length of the plasma column at  $t = 0$  is close to its 'equilibrium length'.

- (ii) The second method assumes that the electron cloud starts from one possible equilibrium state that corresponds to the rigid rotor motion with an angular frequency [12]

$$\omega_E^- = \frac{\omega_{ce}}{2} \left[ 1 - \left( 1 - \frac{2\omega_{pe}^2}{\omega_{ce}^2} \right)^{\frac{1}{2}} \right] \quad (2)$$

where  $\omega_{pe}$  is the electron plasma frequency and  $\omega_{ce}$  is the electron cyclotron frequency.  $\omega_E^-$  is characteristic to an  $E \times B$  rotation of the plasma column.

Figure 4 shows a comparison of the radial electron density profile after about 500 ns for the two methods of initialising the non-neutral plasma. Both initial conditions lead to similar main features: pseudo-flat plateau of the electron density below  $2 \times 10^{14} \text{ m}^{-3}$  with a radius close to 3 cm, and a negative

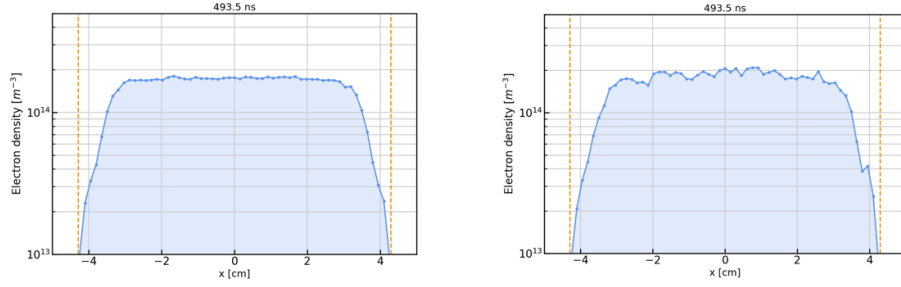


Figure 4: Comparison of the transverse electron density profile after 500 ns for two different initial plasma distributions - thermal equilibrium (left) and rigid rotor motion (right).

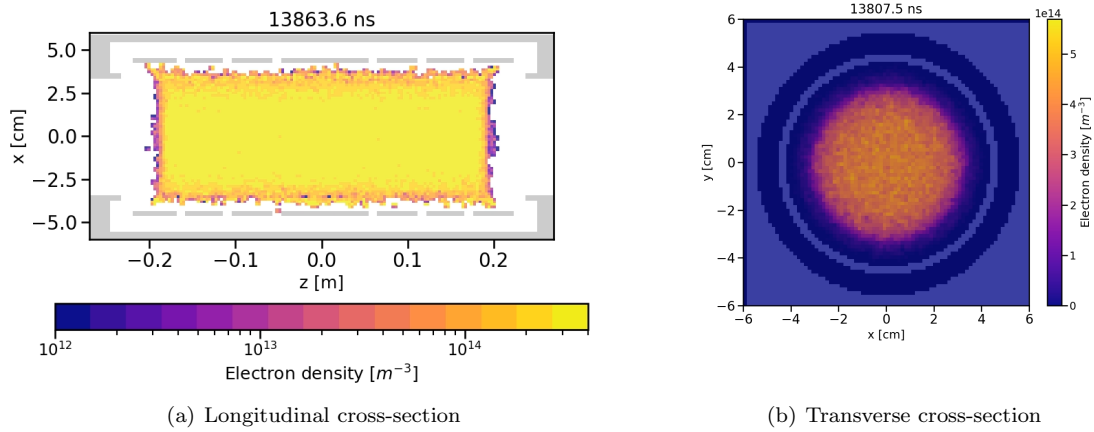


Figure 5: The averaged electron density shows a stable plasma after a time period of more than  $10 \mu\text{s}$ . The effective length of the electron cloud is reduced compared to the length of the central anode as the edges of the plasma follow the shape of the field lines.

radial gradient near the inner surface of the anode. Initial thermal equilibrium leads to a more uniform density plateau, while the initial rigid rotor state results in a more non-uniform density distribution on the time scale considered here.

**Observations** Figures 5 and 7 show a typical electron cloud under a stable regime after more than  $10 \mu\text{s}$ . The electron cloud has a radial extension smaller than the anode radius. A pseudo-flat plateau is observed at  $\sim 60\%$  of nominal electron density between  $\pm 2 \text{ cm}$ . The negative radial gradient of the electron density is consistent with a stable plasma. In the transverse plane, the plasma is rotating azimuthally around the central axis of the lens. The electrons are lost from the two ends of the plasma column and near the inner surface of the anode in the first 20 ns. Figure 6 shows a high spike in the absorbed electron current at the inner surface of the central electrode during the first 20 ns of the simulation. No electrons were registered to have reached the end planes of the lens or the walls of the outer vacuum vessel.

## 2.2 Unstable regime

The images of the ring-shaped beams taken during the experimental test of the prototype of the lens suggest an electron cloud which was rotating around the beam axis and which had a non-zero radial density gradient. Several initial electron distributions were investigated in the simulations to identify the plasma dynamics that leads to ring-like beam spots. For the initial conditions, the velocity of the electrons were defined according to the rigid rotor state described in the previous section.

### 2.2.1 Beam tracking

The main aim of the numerical studies was to investigate the effect of the plasma instabilities on a proton beam traversing the lens. For this purpose, an instability was let to develop inside the lens and then the

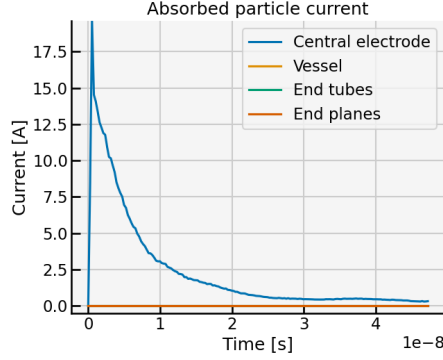


Figure 6: The absorbed electron current at the surface of the components of the lens as a function of time.

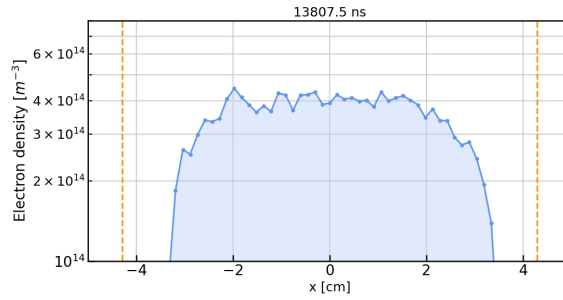


Figure 7: Longitudinally averaged electron density vs. transverse dimension for the lens prototype. as simulated with VSim. The dashed vertical lines indicate the inner edges of the lens anode.

pencil beams were transported through the electron cloud simultaneously with the instability evolving. Tracking the pencil beams through the lens was done in two stages:

- (i) The beamlets were propagated through the electron plasma using VSim.

The 1.4 MeV protons were generated at the entry plane of the lens using the available particle loader in VSim. The macroparticles were placed according to a bit-reversed algorithm as provided by VSim. The beamlets have a radius of 1 mm, no angular divergence, and their position was determined from the aperture used in the experimental test of the lens. Each pencil beam was continuous corresponding to a current of  $0.5 \mu\text{A}$ . A screen of the type *Absorbed Particle Log* was introduced at the exit plane of the lens to record the  $(x, y, z, z', y', z')$  coordinates of all the macroparticles that exit the lens through the beam-pipe. In order to get high statistics for the proton beams, 30 macroparticles were generated during each time step.

- (ii) The beamlets were tracked through an additional drift space of 67 cm using BDSIM.

During the experiment, the intensity of the beamlets was recorded on a phosphor screen 67 cm downstream of the lens. To simulate the profile of the beamlets at the same position along the beamline, the protons were propagated through an additional drift space in BDSIM which is more computationally efficient for this task compared to the the PIC code .

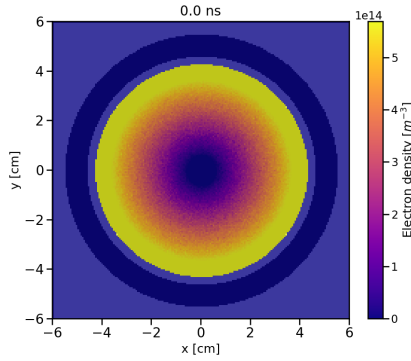
The more significant instabilities observed in the simulations and their effect on the pencil beams are presented below.

### 2.2.2 Diocotron instability

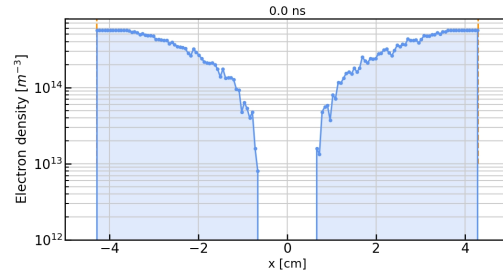
The most common type of instability in low density non-neutral plasmas which has been observed experimentally [13, 14] and in numerical simulations [15] is the diocotron instability [16]. It is known that the diocotron instability is driven by high positive radial gradients in the electron density [12]. As a verification of how the simulation parameters had been set up for the lens under investigation, an initial simulation was run with a very large radial density gradient shown in Figure 8 for which the diocotron

Table 1: Main parameters used for simulating the plasma in the stable regime

Parameter	Value
Current in the coil (I)	20 A
Average magnetic field ( $B_{avg}$ )	20.4 mT
Anode potential ( $V_A$ )	17 kV
End electrodes potential	0 kV
Maximum theoretical electron density ( $n_{e,max}$ )	$2 \times 10^{15} \text{ m}^{-3}$
Initial filling factor	10 %
Number of steps per plasma period	30
Grid size	$12 \text{ cm} \times 12 \text{ cm} \times 54 \text{ cm}$
Number of cells in each direction	$200 \times 200 \times 160$
Macroparticles per cell	10
Background gas ( $\text{H}_2\text{O}$ ) pressure	$5 \times 10^{-6} \text{ mbar}$



(a) Transverse cross-section



(b) Transverse electron density profile.

Figure 8: Initial electron distribution that leads to the diocotron instability.

instability should have been observed. Figure 9 shows the formation of such an instability on a time-scale of  $1 \mu\text{s}$ . The instability can be easily recognised by the vortices that form on the edge of the electron ring.

The effect of the diocotron instability on an ion beam is shown in Figure 10(a). Eight circular pencil beams with an initial diameter of 2 mm enter the plasma at  $1 \mu\text{s}$  and the beams are continuous for the rest of the simulation. The beam spots as imaged on a screen 67 cm downstream of the lens show a smearing of the pencil beams across elliptical spots with roughly constant intensity. There is no indication of formation of rings.

### 2.2.3 Electron ring

Decreasing the radial density gradient leads to a more stable plasma distribution. For the particular initial electron density shown in Figure 11 the plasma evolves as a ring which rotates around the central axis. The ring remained stable during the full  $10 \mu\text{s}$  time interval of the simulation. However, the plasma ring is highly symmetric and cannot lead to ring-like beam spots, as seen in Figure 10(b).

When the annular plasma instability forms in the first part of the simulation, the electron ring has a 4-fold symmetry which is lost due to the subsequent rotation of the ring around the central axis. Since the central anode has four longitudinal sets of holes to maintain a good vacuum, these apertures could act as a source of electron loss and cause the 4-fold symmetry. However, a separate simulation was run with the identical initial conditions and no holes in the anode which leads to the same instability being observed.

### 2.2.4 ‘Dipole instability’

To introduce an asymmetry in the electron distribution, the initial plasma column was offset with respect to the central axis of the lens by 1 cm. In addition, the plasma column was initially set to rotate around the beam axis with a period of 100 ns. The rotation of the plasma and the positive radial gradient of

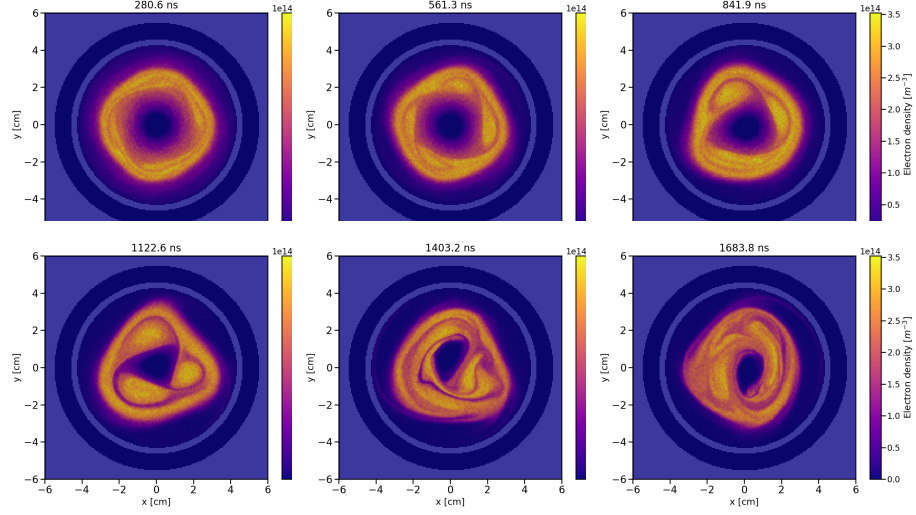


Figure 9: Diocotron instability as seen in a transverse cross-section through the anode of the lens.

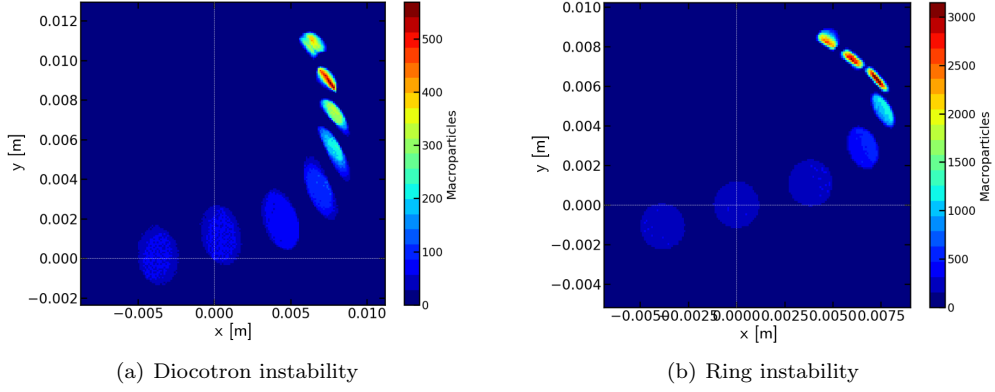


Figure 10: Number of macroparticles hitting a screen 67 cm downstream of the lens. The eight circular pencil beams passed through the corresponding instability.

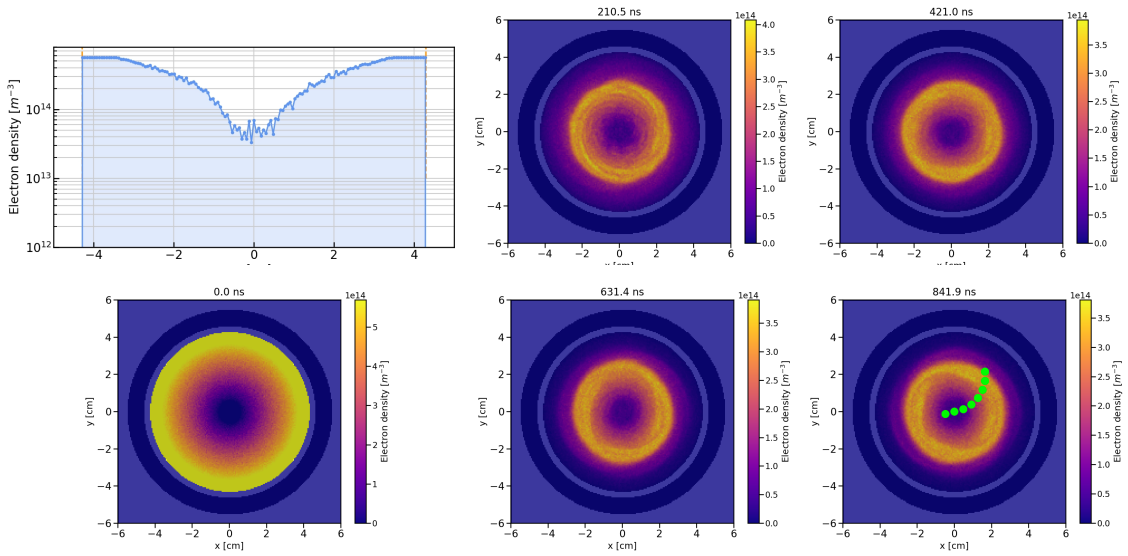


Figure 11: Initial electron density profile and the subsequent evolution of the plasma as an electron ring. The green spots mark the entry position of the pencil beams.



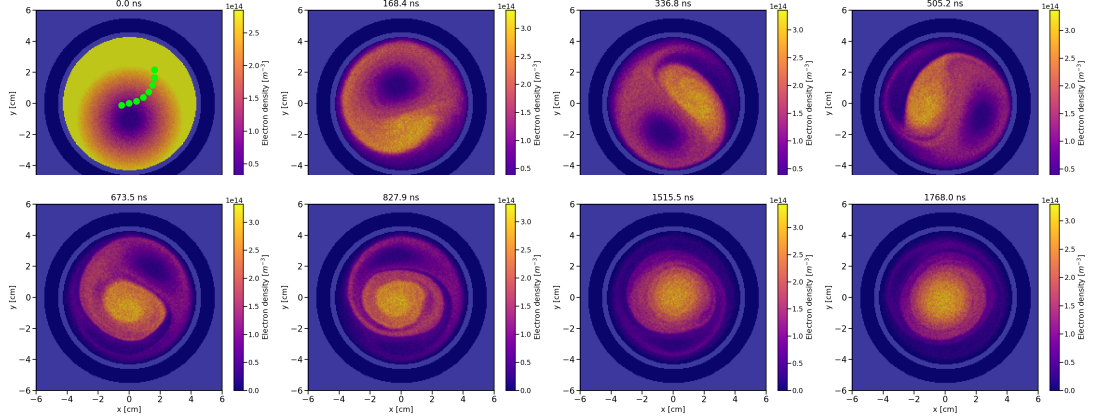


Figure 12: ‘Dipole instability’ as seen in a transverse cross-section through the anode of the lens. The green spots mark the entry position of the pencil beams.

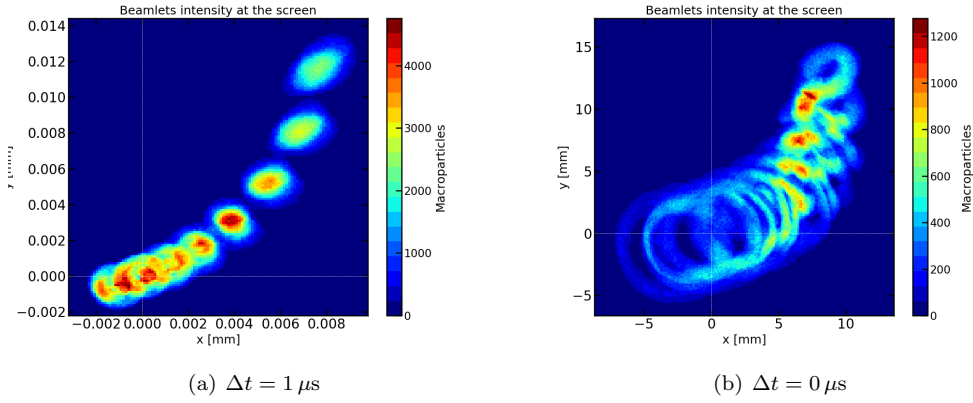


Figure 13: Number of macroparticles hitting a screen 67 cm downstream of the lens. The eight circular pencil beams passed through the ‘dipole instability’. The protons entered the lens at a time  $\Delta t$  after the initialisation of the plasma.

the electron density lead to a dipole structure: two regions of low and high electron density, respectively. Figure 12 shows the dipole structure rotating around the beam axis with the instability gradually being damped. After about  $2 \mu s$  the electron cloud becomes more uniform and centred around the beam axis.

Figure 13(b) shows the intensity of eight pencil beams that propagate through the ‘dipole instability’. The protons enter the plasma starting at  $t = 0$  ns. Since the size of the high density region changes together with its offset from the axis, several rings appear superimposed for each pencil beam. The radius of the rings decreases and the eccentricity increases for the pencil beams that propagate further away from the central axis of the lens.

Figure 13(a) shows an absence of the ring spots if the pencil beams enter the instability at a later time when the dipole structure has become more uniform. One possible driving mechanism for the instability may be the electron streams which are produced at the surface of the end electrodes due to the high voltage. Such electron streams may both feed the high density region and maintain its rotation if they enter the magnetic field with high enough angular momentum.

### 3 Alternative model of the instability

To reproduce the images taken during the experimental test of the space-charge lens built at Imperial and to better understand the instability, a model was created based on the main features of the non-neutral plasma that was seen to lead to ring-like beam spots. The goal was to create a tool that reproduces the effect of the instability on the pencil beams that pass through the plasma with a significantly reduced

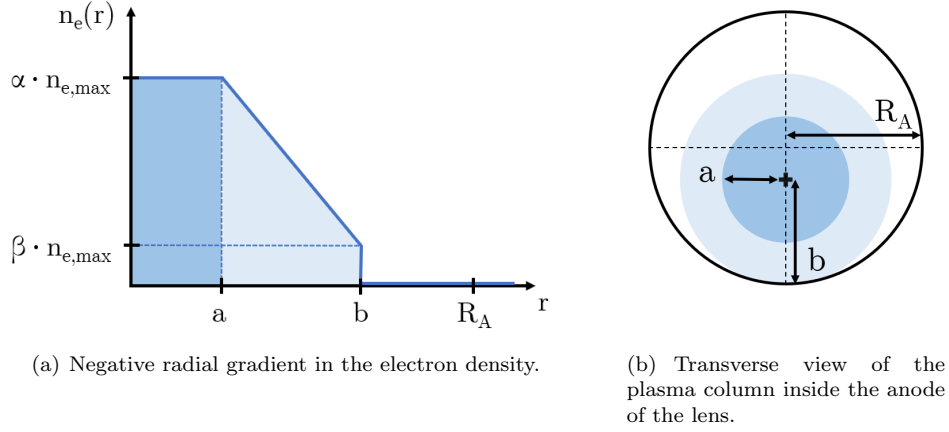


Figure 14: Radial electron density profile.  $R_A$  represents the radius of the lens anode and  $n_{e,\max}$  is the theoretical maximum electron density.  $r$  is measured from the centre of the plasma column. The profile is fully described by the parameters  $\alpha, \beta, a$ , and  $b$ .

computation time compared to VSim. Thus, a wider parameter space was investigated for the plasma.

### 3.1 Electric field map

One method to model the instability observed in earlier simulations is to describe the electron cloud using a simplified charge distribution which preserves some of the more important features. Such a charge distribution should be simple enough to allow the electric field to be calculated based on Gauss's law if we neglect end effects and the potential of the anode. Once the electric field is calculated, a discrete 3D field map can be generated and used to model the electron cloud for particle tracking.

The radial profile chosen for the electron density is shown in Figure 14 and it is given by

$$\frac{n_e(r)}{n_{e,\max}} = \begin{cases} \alpha, & r < a \\ mr + c, & a \leq r \leq b \\ 0, & b < r < 2R_A \end{cases} \quad (3)$$

where  $m, c$  are functions of  $\alpha, \beta, a, b$  given that  $n_e(a) = \alpha \cdot n_{e,\max}$  and  $n_e(b) = \beta \cdot n_{e,\max}$ .  $r$  is the radial coordinate measured from the centre of the plasma column. Here,  $b$  acts as a cut-off radius - its value is always set such that the electron density drops to zero where the plasma column touches the inner surface of the anode if an offset is introduced between the central axis of the plasma column and the central axis of the lens. Thus, the electron cloud maintains the cylindrical symmetry for any radial offset of the plasma column. Neglecting the end effects, the radial electric field was obtained from equation (3)

$$E_r = -\frac{en_{e,\max}}{2\epsilon_0} \begin{cases} \alpha r, & r < a \\ \frac{2}{r} \left[ \frac{\alpha a^2}{2} + \frac{m}{3} (r^3 - a^3) + \frac{c}{2} (r^2 - a^2) \right], & a \leq r \leq b \\ \frac{2}{r} \left[ \frac{\alpha a^2}{2} + \frac{m}{3} (b^3 - a^3) + \frac{c}{2} (b^2 - a^2) \right], & b < r < 2R_A \end{cases} \quad (4)$$

From the earlier plasma simulations done with VSim, we observed that such a plasma column rotates around the lens axis with a period of the order of 100 ns. Both the total time interval for which the field map is specified and the spatial and temporal resolutions are limited by the computation time. The total time interval for which the field map is generated can be increased if the spatial resolution is decreased, keeping the total memory size required by the field map constant. The field map was generated to include at least three periods of rotation and up to ten periods by modifying the spatial resolution accordingly. Increasing the resolution of the field map increases the time it takes to generate the field map as well as the duration of the beam tracking. Thus, we chose a time step  $dt = 0.2$  ns and a spatial grid separation of 0.5 mm. No significant change was observed in the beam tracking for shorter time steps or better spatial resolution.

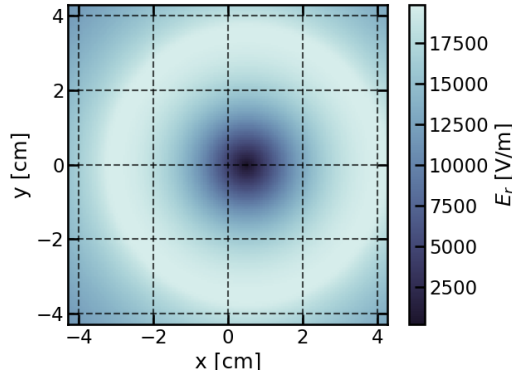


Figure 15: Example of an electric field map (transverse view) generated from the electron distribution shown in Figure 14 for  $n_{e,max} = 1 \times 10^{14} \text{ m}^{-3}$ ,  $a = 1 \text{ cm}$ ,  $\alpha = 1$ ,  $\beta = 0.1$  and a horizontal offset of 0.5 cm.



Figure 16: Experimental arrangement reproduced as a beamline in BDSIM. The orange rectangle shows the region occupied by the electric field map with a length of 36 cm. The phosphor screen is placed 67 cm downstream of the Gabor lens.

### 3.2 Particle tracking

A particle tracking code BDSIM was used to study the effect of the idealised time-dependent electron distributions on a proton beam passing through the lens. BDSIM has the option to load a time-dependent electric or magnetic field map inside a predefined volume. From the interpolators provided with the code, we chose a 4D cubic interpolator. Figure 16 shows the position of the phosphor screen 67 cm downstream of the Gabor lens. An additional drift space was introduced before and after the lens to account for the fact that the effective length of the electron cloud is smaller than the full length of the lens (50 cm). As observed previously in the plasma simulations done with VSim, the electron cloud (36 cm) almost fully occupies the length of the central anode (44.4 cm).

The input proton distribution was loaded into BDSIM by using a file that is generated separately. The file specifies the  $(x, x', y, y', t, E)$  coordinates of each particle at the input plane. The  $x, y$  coordinates were generated to fill uniformly six circular holes of radius  $r = 1 \text{ mm}$ . The position of the holes is chosen based on the aperture placed upstream of the Gabor lens during the experiment. All the protons had an energy of 1.4 MeV and the beam duration was set to 300 ns such that it samples several rotations of the electron cloud. The  $x'$  and  $y'$  were tuned such that the intensity profile of the six beamlets at the screen as obtained with BDSIM matches the images taken during the experiment with the lens off. These profiles were matched in terms of the relative position of the beamlets, as well as the  $x$ - and  $y$ -diameter of each spot as illustrated in Figure 17. The resulting phase space is shown in Figure 18.

### 3.3 Results

To verify the stability of a plasma column described by the model in Figure 14, the same density profile was used to initialise an electron cloud in VSim. The plasma column maintains the negative radial gradient and rotates around the central axis of the lens with a period between 200 ns and 300 ns. However, the radius of rotation gradually decreases as the plasma becomes circularly symmetric after about  $1 \mu\text{s}$  (see Fig. 19). Therefore, such a rotation of the plasma column is expected to persist only in

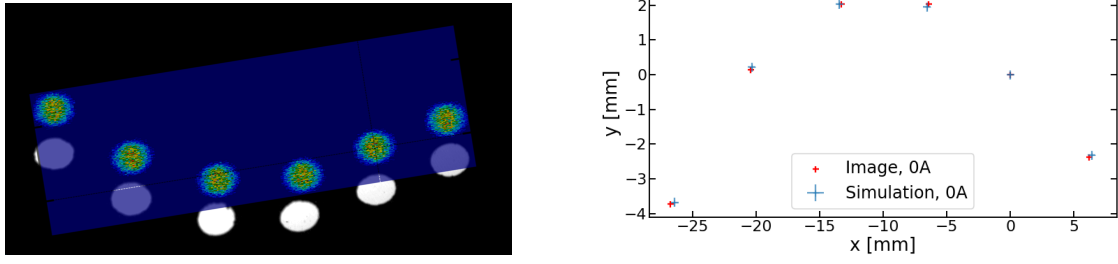


Figure 17: (Left) Image of the six beam spots on the screen when the lens was turned off. A reproduction of this pattern is overlapped on top of the image with a vertical shift. The divergence of the beamlets is tuned to ensure that the position, orientation, and size of the spots match with the image. (Right) Position of the centroid of each beam spot for a current of 0A in the coil of the lens as extracted from image and simulation. In the case of the simulation, the size of each marker represents the error.

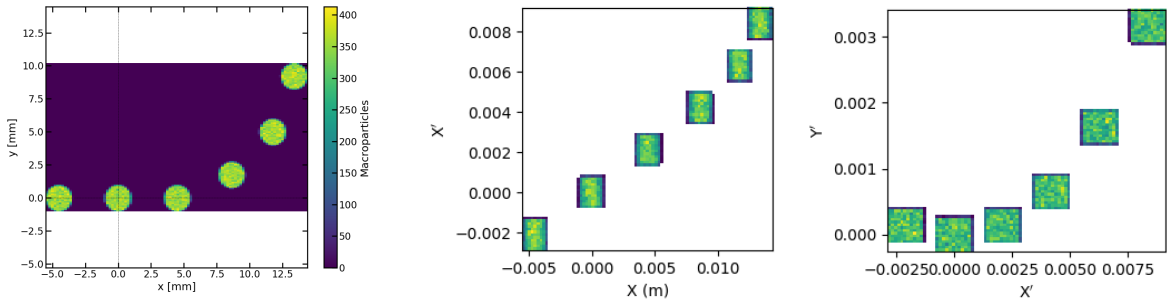


Figure 18: Phase space of the six beamlets at the entry plane of the Gabor lens.

the presence of a driving mechanism, such as electrons streaming from the surface of the end electrodes.

When the free parameters of the model (maximum electron density  $n_{e,\max}$ , peak width  $a$ , radius of rotation, and period of rotation) were tuned accordingly, a qualitative agreement was obtained between the images taken during the experiment for a coil current of 32 A and the results of the simulation shown in Figure 20(a). Furthermore, the model predicts the same change in the intensity pattern of the pencil beams as the experiment when the current is increased in the coil from 18 A to 32 A. Similarly to the experiment, Figure 21 shows that the rings start to form for a current of 28 A or above. To obtain the qualitative agreement, the filling factor of the lens was set to 4%. This value was obtained from the theoretical electron density predicted from the average magnetic field associated to each value of the coil current.

Figure 23 shows that increasing the maximum electron density  $n_{e,\max}$  in the central region of the plasma column decreases the separation between the rings and the thickness of the ring due to stronger focusing. Moreover, the aspect of the spots changes significantly with a small variation of the electron density. Thus, matching the pattern from a simulation to an image taken during the experiment provides

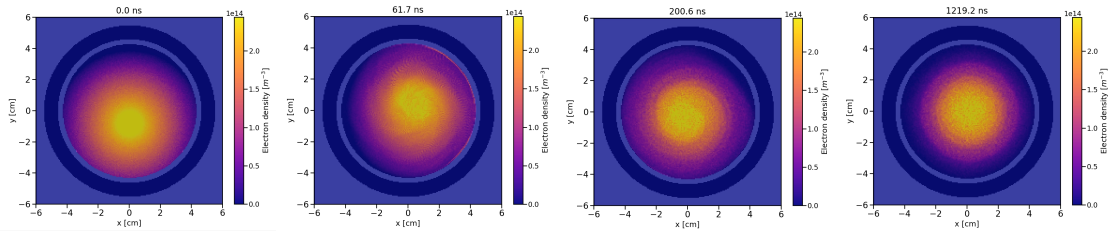


Figure 19: Evolution of the idealised electron cloud described in Fig. 8(b) simulated with VSim. In the absence of a driving mechanism, the radius of rotation of the plasma column around the beam axis gradually decreases until the space-charge becomes circularly symmetric after a time scale of  $1 \mu\text{s}$ .

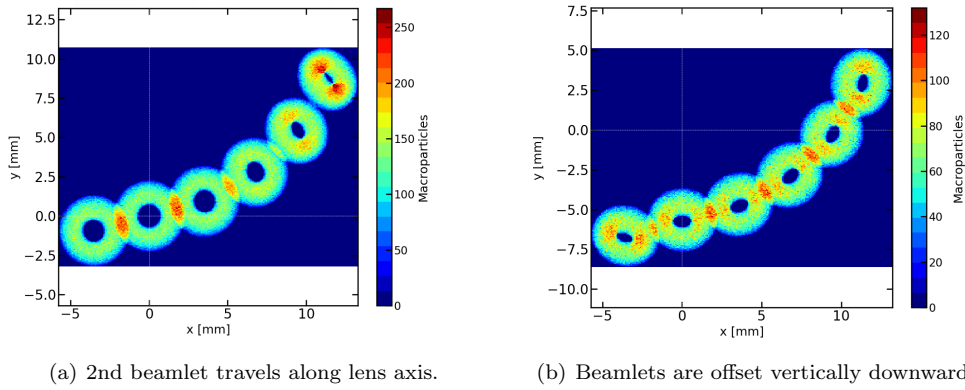


Figure 20: Number of macroparticles hitting the screen for an idealised rotating electron plasma as simulated with BDSIM. The separation between the rings and the eccentricity of each ring increases further away from the axis of the lens. The shape of the rings is also affected by a possible offset between the beam axis and the axis of rotation of the plasma column.

an evaluation of the density of the plasma that was confined in the lens during the measurements. However, Figure 22 shows that a similar change in the radius of the rings was obtained by increasing the radius of rotation of the plasma column around the central axis. This result suggests that matching a simulation to an image from the experiment may not be a one-to-one mapping.

By looking at how the rate of rotation of the plasma affects the formation of the rings, Figure 24 suggests a lower limit for the rotation period. In order for the rotation of the plasma not to be averaged out during the transit time of the protons, the rotation period needs to be high enough. A rotation period which is at least a factor of five higher than the transit time of the beam is necessary for the formation of clear rings.

If the radius of rotation of the plasma and the filling factor remain constant while changing the current through the coil of the lens, certain trends appear. The linear focusing force is depicted in Figure 25(a) which shows that the centroids of the ring spots move towards the focusing centre for higher electron densities. The six sets of points, each for the corresponding pencil beam, point back to the same focusing centre. This feature does not appear in the experimental data which suggests that the rotation of the plasma column may have been affected when the current in the coil was increased between consecutive measurements.

A second general trend is indicated in Figure 25(b). The eccentricity of each ring is seen to increase for higher electron densities. The beam spots which are further away from the central axis have a higher eccentricity for each value of the current, and they also span a wider range of values.

## 4 Conclusion

A PIC code was used to simulate the stable operation of the first prototype of the Gabor lens built at Imperial. The results helped to understand how the geometry of the lens affects the distribution of the space-charge. For the unstable regime, both the PIC code and a particle tracking code were used to study the effect of different instabilities on six pencil beams that pass through the plasma. An instability with dipole structure was associated with the formation of ring spots from the pencil beams. A simplified model was created with the essential features of the dipole instability. The model lead to a reproduction of the images taken during the experimental test of the prototype.

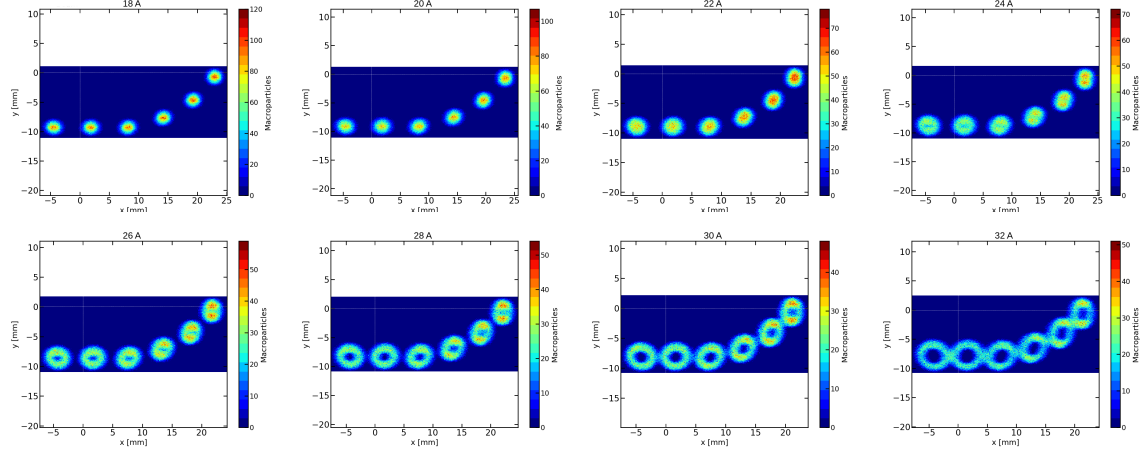


Figure 21: Intensity pattern for the six pencil beams passing through the idealised rotating plasma column for the lens current increasing from 18 A to 32 A. A filling factor of 4% was assumed for the lens.

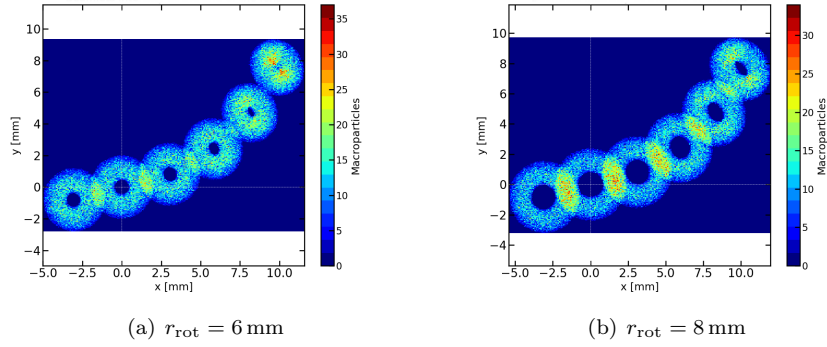


Figure 22: The effect of increasing the radius of rotation of the plasma column around the central beam axis on the appearance of the ring spots.

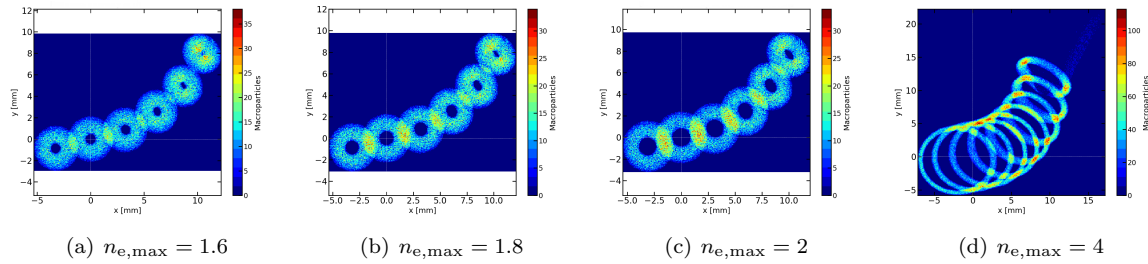


Figure 23: The effect of increasing the maximum electron density on the appearance of the ring spots.  $n_{e,\text{max}}$  is given in units of  $10^{14} \text{ m}^{-3}$ . In case (d), eight pencil beams were simulated.

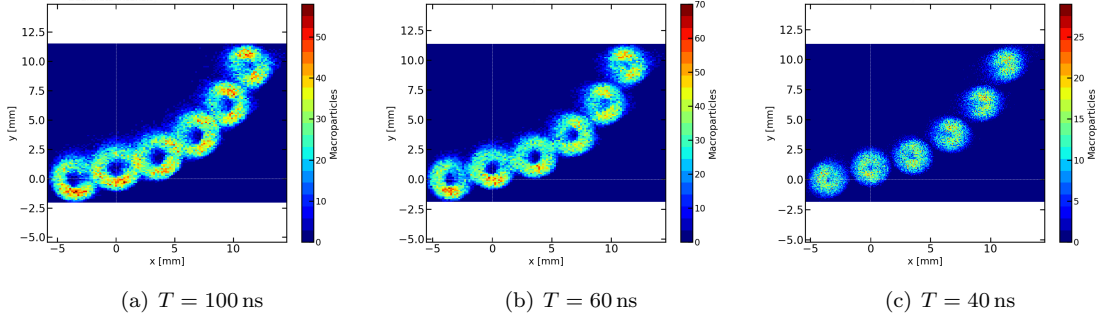


Figure 24: Decreasing the period of rotation of the plasma column leads to incomplete ring formation for the beamlets that are further away from the central axis. The ring-like aspect becomes clearer when the period of rotation is by at least a factor of 5 larger than the beam transit time through the lens ( $\approx 20$  ns).

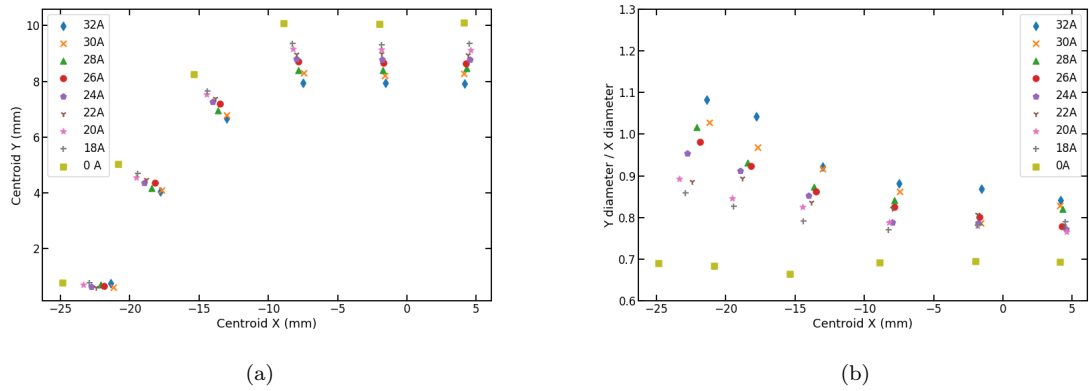


Figure 25: Variation of the position of the centroid and the ratio of y-diameter over the x-diameter for the ring spots when increasing the current through the coil of the lens. For each current, a different field map was generated and used for tracking the pencil beams through the lens.

## References

- [1] J. Pozimski, R. Dölling, P. Gross, and H. Klein, “Investigation of space charge compensated transport by use of a gabor plasma lens,” 01 1996.
- [2] M. Droba, B. Glaeser, S. Klaproth, O. Meusel, U. Ratzinger, and K. Schulte, “Studies on Electron Cloud Dynamics for an Optimized Space Charge Lens Design,” *Conf. Proc. C*, vol. 110904, pp. 3495–3497, 2011.
- [3] K. Schulte, M. Droba, O. Meusel, and U. Ratzinger, “Investigation of diagnostic techniques on a nonneutral plasma,” in *Proceedings of the 10th European Workshop on Beam Diagnostics and Instrumentation for Particle Accelerators DIPAC2011, Hamburg, Germany, 2011*, no. MOPD93, pp. 266 – 268, 2011.
- [4] P. Posocco, M. Merchant, J. Pozimski, and Y. Xia, “First Test of The Imperial College Gabor (Plasma) Lens prototype at the Surrey Ion Beam centre,” in *Proc. of International Particle Accelerator Conference (IPAC’16), Busan, Korea, May 8-13, 2016*, no. 7 in International Particle Accelerator Conference, (Geneva, Switzerland), pp. 1598–1600, JACoW, June 2016.
- [5] “Vsim for plasma,” 2020. <https://www.txcorp.com/vsim>.
- [6] L. J. Nevay *et al.*, “Bdsim: An accelerator tracking code with particle-matter interactions,” *Computer Physics Communications*, p. 107200, 2020.
- [7] “Finite Element Method Magnetics (FEMM).” <http://www.femm.info/wiki/HomePage>.
- [8] M. Reiser, “Comparison of gabor lens, gas focusing, and electrostatic quadrupole focusing for low-energy ion beams,” in *Proc. of the 1989 IEEE Ptcl. Acc. Conf., . ’Accelerator Science and Technology*, pp. 1744–1747 vol.3, 1989.
- [9] “Electron-Impact Cross Sections for Ionization and Excitation, NIST,” 2020. <https://physics.nist.gov/PhysRefData/Ionization/molTable.html>.
- [10] Y. Itikawa and N. Mason, “Cross sections for electron collisions with water molecules,” *Journal of Physical and Chemical Reference Data*, vol. 34, no. 1, pp. 1–22, 2005.
- [11] “Scientific Computing Resources for Facilities,” 2020. <https://www.scarf.rl.ac.uk/home>.
- [12] R. C. Davidson, *Physics of nonneutral plasmas*. Imperial College Press London, 2001.
- [13] C. A. Kapetanacos, D. A. Hammer, C. D. Striffler, and R. C. Davidson, “Destructive instabilities in hollow intense relativistic electron beams,” *Phys. Rev. Lett.*, vol. 30, pp. 1303–1306, Jun 1973.
- [14] G. Rosenthal, G. Dimonte, and A. Y. Wong, “Stabilization of the diocotron instability in an annular plasma,” *The Physics of Fluids*, vol. 30, no. 10, pp. 3257–3261, 1987.
- [15] O. Meusel, M. Droba, B. Glaeser, and K. Schulte, “Experimental studies of stable confined electron clouds using Gabor lenses,” *AIP Conf. Proc. C*, vol. 1206051, pp. 157–160. 4 p, Sep 2013. Comments: 4 pages, contribution to the Joint INFN-CERN-EuCARD-AccNet Workshop on Electron-Cloud Effects: ECLOUD’12; 5-9 Jun 2012, La Biodola, Isola d’Elba, Italy.
- [16] R. H. Levy, “Diocotron instability in a cylindrical geometry,” *The Physics of Fluids*, vol. 8, no. 7, pp. 1288–1295, 1965.